MATERIALS SCIENCE

Experimental and theoretical evidence for molecular forces driving surface segregation in photonic colloidal assemblies

Ming Xiao[1*†], Ziying Hu[2*], Thomas E. Gartner III[3*], Xiaozhou Yang[1‡], Weiyao Li[1], Arthi Jayaraman[3,4§], Nathan C. Gianneschi[2§], Matthew D. Shawkey[5§], Ali Dhinojwala[1§]

Surface segregation in binary colloidal mixtures offers a simple way to control both surface and bulk properties without affecting their bulk composition. Here, we combine experiments and coarse-grained molecular dynamics (CG-MD) simulations to delineate the effects of particle chemistry and size on surface segregation in photonic colloidal assemblies from binary mixtures of melanin and silica particles of size ratio (D_{large}/D_{small}) ranging from 1.0 to ~2.2. We find that melanin and/or smaller particles segregate at the surface of micrometer-sized colloidal assemblies (supraballs) prepared by an emulsion process. Conversely, no such surface segregation occurs in films prepared by evaporative assembly. CG-MD simulations explain the experimental observations by showing that particles with the larger contact angle (melanin) are enriched at the supraball surface regardless of the relative strength of particle-interface interactions, a result with implications for the broad understanding and design of colloidal particle assemblies.

INTRODUCTION

Self-assembly of colloidal particles produces structural materials for a broad range of applications such as metamaterials (*1*), solar cells (*2*), photonic sensors (*3*), and drug delivery (*4*). In most of these applications, the assembly of colloids results in structural colors that are more resistant to chemical washing or photobleaching than pigment-based colors (*5*, *6*). The current state-of-the-art structural colors from colloidal assemblies are mostly constrained to film geometries using evaporation-induced assembly (*7*), electrophoretic deposition (*8*), and spray coating (*9*). These films are difficult to apply as "pigment-like" colorants that can be directly added to other materials such as paints or textiles. Furthermore, the interference-based structural colors on flat substrates are mostly iridescent, limiting their use in wide-angle display or accurate sensing applications. Recently, a simple approach involving self-assembly of colloidal nanoparticles in emulsion droplets was used to fabricate photonic micrometer-sized spheres (termed supraballs) made of close-packed nanoparticles (*10*). The colors of supraballs are independent of rotation under fixed illumination and can be used as wide-angle photonic inks and additives in cosmetics, paints, and sensors (*11*–*14*). Thus, controlling the composition and structure of supraballs is critical for tuning optical properties for broad applications.

Binary particle mixtures enable rich structures and properties of colloidal assemblies. For example, binary mixtures break long-range order of colloidal crystals, leading to non-iridescent colors (*15*, *16*). Precise tuning of the size ratio of the binary particles can produce diverse types of colloidal crystals (*17*), and changing the volume ratios of binary particle mixtures can tune the structural colors of the assemblies (*18*). In addition, the use of two particle types allows selective removal of one component, leading to porous structures with controlled disorder (*19*).

The use of binary particles in supraball assembly not only enhances properties for application but also has fundamental significance. The packing of binary colloidal nanoparticles within a spherical template has critical fundamental relevance in understanding crystal growth on curved surfaces, yet is not well understood (*20*–*22*). Furthermore, the spatial organization of nanoparticles in the top few layers of the assembled supraballs (where most light is scattered) is critical to tune application-oriented properties such as the wavelength of structural colors (*11*, *23*) or selective binding for drug delivery (*24*). Mixtures of two or more types of nanoparticles can lead to additional control over the surface composition and separation between particles, potentially tuning the absorption and contrast. It is thus critical to understand how and why binary nanoparticles assemble at surfaces/interfaces. Stratification of binary mixtures of varying particle sizes during evaporative film formation has been studied via both experiments and simulations (*25*–*32*); these studies have comprehensively mapped the set of particle size ratios, evaporation rates, and mixture compositions to either encourage or suppress surface stratification in films composed of particles with the same surface chemistry. However, to the best of our knowledge, no such complementary work exists for particle mixtures of varying chemistry or for the emulsion assembly process. Similarly, there is no in-depth understanding of the relationship between stratification in supraballs and structural colors. Thus, a systematic variation of nanoparticle size, chemistry, mixture composition, and evaporative versus emulsion assembly processes will offer insights into how we can tailor the particle spatial organization to achieve target structural colors and/or bioactive properties.

To this end, here we use synthetic melanin particles (SMPs) and silica particles (SPs) as two model particles owing to their special optical property and biocompatibility. SMPs have a unique combination of a high refractive index (~1.74) and a broadband absorption (*33*), and SPs have a relatively low refractive index (~1.45) and negligible absorption in the visible region. We investigate the assembly of binary

[1]Department of Polymer Science, The University of Akron, Akron, OH 44325, USA. [2]Department of Chemistry, Northwestern University, Evanston, IL 60208, USA. [3]Department of Chemical & Biomolecular Engineering, University of Delaware, Newark, DE 19716, USA. [4]Department of Materials Science & Engineering, University of Delaware, Newark, DE 19716, USA. [5]Evolution & Optics of Nanostructures Group, Department of Biology, Ghent University, Ghent 9000, Belgium.
*These authors contributed equally to this work.
†Present address: Harvard John A. Paulson School of Engineering and Applied Sciences, Harvard University, Cambridge, MA 02138, USA.
‡Present address: Department of Chemistry, Virginia Polytechnic Institute and State University, 800 West Campus Drive, Blacksburg, VA 24061, USA.
§Corresponding author. Email: ali4@uakron.edu (A.D.); matthew.shawkey@ugent.be (M.D.S.); nathan.gianneschi@northwestern.edu (N.C.G.); arthij@udel.edu (A.J.)

particles varying in particle size (D_{large}/D_{small} ranging from 1.0 to ~2.2) and composition using two techniques, reverse emulsion assembly of supraballs and evaporative assembly of flat films. In the reverse emulsion supraball assembly, for mixtures with the same bulk volume fraction of small and large SPs, the smaller SP particles cover 78 to 89% of the supraball surface, and for mixtures with the same size SMPs and SPs, SMPs occupy almost 100% of the supraball surface. By contrast, in the evaporative assembly of flat films, the surface composition of the films of analogous systems mimics the bulk material composition. Interfacial tension measurements, particle-interface contact angle experiments, and coarse-grained molecular dynamics (CG-MD) simulations show that the trends in surface segregation in the supraballs are driven by the geometry (i.e., contact angle, smaller particles more easily accommodate the curvature of the supraball surface) of the particles at the liquid/liquid interface during supraball assembly. Furthermore, the differences between supraball and thin-film assembly stem from dissimilar particle interactions with the water/1-octanol interface (supraballs) and water/air interface (films).

RESULTS AND DISCUSSION

Supraballs from binary mixtures of particles

To investigate how mixtures of binary particles affect the structure and optical properties of assembled supraballs, we have prepared three sizes of SPs (diameter, 139 ± 9, 219 ± 11, and 299 ± 10 nm) and SMPs (diameter, 137 ± 15, 217 ± 16, and 298 ± 22 nm). These particles are well dispersed in water and have similar negative zeta potentials in water (table S1). We fabricated nine types of binary supraballs using the same bulk volume fraction of SPs and SMPs through a one-pot reverse emulsion assembly process (*11*). Specifically, a mixture of SP and SMP aqueous solutions with a filling volume fraction of 0.03 was dispersed in an anhydrous 1-octanol continuous phase, followed by the formation of water-in-oil reverse emulsions using a vortex mixer (fig. S1). Because of the slight solubility of water in 1-octanol, water diffused from the droplets into the 1-octanol phase, causing the colloidal droplets to shrink and finally assemble to solid supraballs. The assembly process took ~5 min.

Figure 1 shows scanning electron microscopy (SEM) images of surfaces of nine types of supraballs. Using the contrast due to the differences in the particle size and brightness between SPs and SMPs (silica is brighter than melanin under SEM), we can distinguish the chemical identity of the particles at the supraball surfaces. SMPs with diameters of 137 and 217 nm cover nearly 100% of the supraball surfaces when they are mixed with all three sizes of SPs (Fig. 1, A to F), and 298-nm SMPs also fully cover the supraball surface when mixed with 299-nm SPs (Fig. 1I). It is difficult to precisely quantify the SMPs' volume fraction at the supraball surface layer (here termed "surface volume fraction") for those three cases, because the particle tracking algorithm does not work accurately owing to lower image quality caused by charging effect. The surface segregation analysis was conducted for 10- to 20-μm-diameter supraballs throughout this paper.

When mixing 298-nm SMPs with smaller SPs (139 or 219 nm), both SMPs and SPs are present at the supraball surfaces (Fig. 1, G and H). The surface volume fraction of SMPs at the outermost layer is 0.58 ± 0.17 for Fig. 1G and 0.46 ± 0.17 for Fig. 1H. These large error values come from the particle tracking analysis when analyzing two sizes of particles with

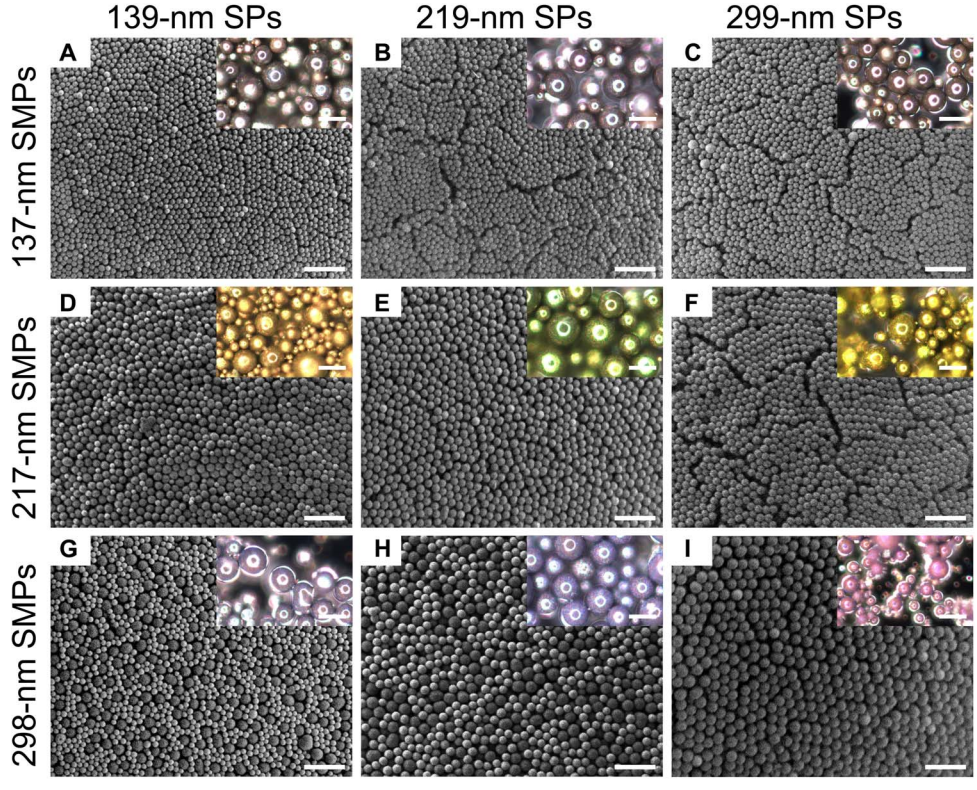

Fig. 1. SEM images of the surface of supraballs made of binary particles with equal bulk volume fraction. (**A**) 139/137-nm SPs/SMPs, (**B**) 219/137-nm SPs/SMPs, (**C**) 299/137-nm SPs/SMPs, (**D**) 139/217-nm SPs/SMPs, (**E**) 219/217-nm SPs/SMPs, (**F**) 299/217-nm SPs/SMPs, (**G**) 139/298-nm SPs/SMPs, (**H**) 219/298-nm SPs/SMPs, and (**I**) 299/298-nm SPs/SMPs. SEM scale bars, 1 μm. All insets are dark-field optical images with scale bars of 50 μm.

different brightness. The colors of nine types of supraballs are subtle (Fig. 1, inset), and their reflectance spectra lack substantial features (fig. S2), indicating amorphous nanostructures. Binary mixtures of particles can break crystalline order and thereby form disordered structures (*16*); therefore, it is reasonable to observe dull colors from these supraballs. The selective segregation of one type of nanoparticles at the supraball surface may lead to tuning their structural colors; thus, it is critical to understand how the surface segregation occurs.

Particle size effects

To investigate how the particle size affects the surface enrichment and colors at supraball surfaces, we mixed two different sizes of SPs with the same bulk volume fraction and assembled them into supraballs. SEM images show more small SPs than large SPs at the supraball surface. Specifically, 139-nm SPs segregate to the surface more than 219- or 299-nm SPs (Fig. 2, A and B) and 219-nm SPs segregate more than 299-nm SPs (Fig. 2C). We quantify the surface volume fraction of small SPs at the supraball surface for different size ratios (SR = D_{large}/D_{small}): 0.78 ± 0.07 for SR = 1.36 (219/299 nm), 0.87 ± 0.02 for SR = 1.58 (139/219 nm), and 0.89 ± 0.02 for SR = 2.15 (139/299 nm) (Fig. 2G). The values of surface volume fraction are remarkably larger than the experimentally used bulk volume fractions (0.50 small SPs), indicating a clear surface enrichment of smaller particles at the supraball surfaces. The fact that surface volume fraction increases as SR increases suggests that a larger difference in the size of SPs enhances supraball surface segregation.

To investigate whether the water/1-octanol interface affects this surface segregation, we used an evaporative assembly approach to assemble binary SPs to films where only air/water interface is involved. This assembly process took about 15 hours with a water evaporation rate of 0.5 mm/hour. The films are ~10 μm thick (fig. S3), and thus, their colors are unaffected by the thin-film interference effect (*34*). SEM images of the films show the presence of both particle sizes (Fig. 2, D to F) at the surface. We quantify the packing of two sizes of particles at film surfaces and find that the surface volume fraction of small SPs ranges from 0.51 to 0.60, regardless of the mixture used (Fig. 2G). This demonstrates that, in the mixtures studied herein, smaller SPs do not segregate at the film surfaces, in contrast to those in the binary SP supraballs. We note that previous work from the literature suggests that increasing the large/small size ratio or modifying the evaporation rate can produce stratification in films (*31*, *32*), but given the moderate small/large size ratios (1.36 to 2.15) and slow evaporation rates in this study, the lack of film stratification is unsurprising.

Binary SP supraballs and films show different colors (Fig. 2, insets), despite the same bulk compositions. This is because the particle size effect leads to enrichment of small particles at the supraball surface. The presence of a higher fraction of smaller particles at the surface affects the degree of order and the color of the scattered light.

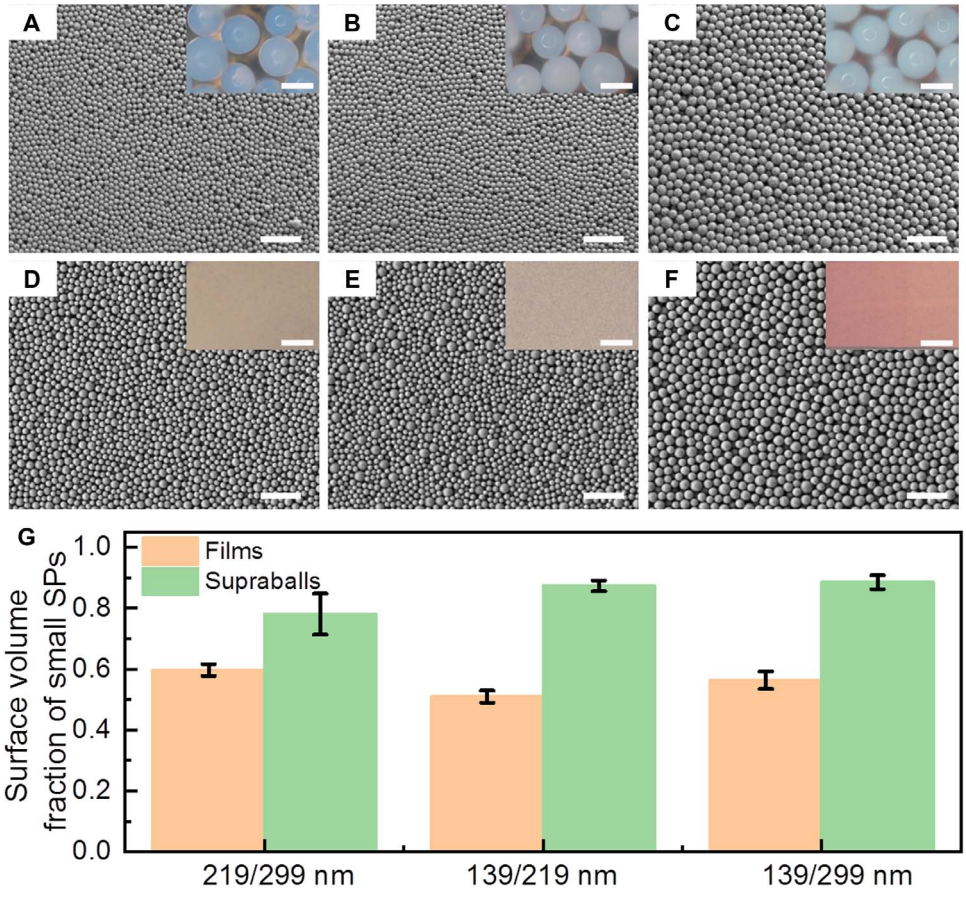

Fig. 2. Supraballs and films from binary SPs. SEM images of the surfaces of supraballs (**A** to **C**) and films (**D** to **F**) made of binary SPs with different sizes and equal bulk volume fraction: (A and D) 139/219-nm SPs, (B and E) 139/299-nm SPs, and (C and F) 219/299-nm SPs. Insets (A to F) are dark-field optical images. SEM scale bars, 1 μm; inset scale bars, 50 μm. (**G**) Surface volume fractions of small SPs for supraballs and films.

Particle chemistry effects

To test how particle chemistry affects surface packing and colors in supraballs and films, we mixed similar-sized SPs and SMPs (average diameter, ~220 nm) with three compositions (bulk volume fractions of SMPs = 0.20, 0.50, and 0.80). SEM images show that the supraball surface is fully covered by one type of particle (Figs. 1E and 3, A and D). Had the surface been a mixture, we would have seen bright and dark particles (as seen in Fig. 1, G and H) owing to the large brightness contrast between SPs and SMPs. The cross-sectional transmission EM (TEM) images of supraballs show that the outermost layer of supraballs is nearly 100% occupied by bright particles and that the inner layers contain a mixture of bright and dark particles (Fig. 3, B and E). Because SPs containing silicon are more electron dense than SMPs under TEM, the outer surfaces of supraballs are completely covered by SMPs even in the mixture with 0.20 bulk volume fraction of SMPs. We further used energy-dispersive x-ray spectroscopy (EDS) imaging to map the silicon element distribution at the same locations as the TEM measurements (Fig. 3, C and F). EDS images confirm that the supraball outer layer is populated with SMPs. Cross-sectional TEM images at random interior positions within the supraballs show random mixtures of the two species (fig. S4). Therefore, we conclude that SMPs strongly segregate at the supraball surfaces (~100% coverage) regardless of bulk volume fraction of SMPs in the mixtures we used here.

In contrast to the supraballs, films made of SMPs and SPs with similar sizes have coverage of both types of particles at the surfaces (Fig. 3, G to I). The surface volume fractions of SMPs are 0.25 ± 0.02, 0.58 ± 0.06, and 0.84 ± 0.04, which are close to the bulk volume fraction for all three cases (0.20, 0.50, and 0.80). Thus, films made of mixtures of SPs and SMPs have no obvious surface segregation, similar to the films made of binary SPs in Fig. 2 (D to F).

The segregation of SMPs at the supraball surfaces notably affects their structural color. Reflectance spectra of supraballs made of mixtures of SPs and SMPs show only moderate variation with the bulk volume fraction of two components due to preference of SMPs over SPs at the interface (fig. S5a). The top layer of the supraballs plays a significant role in the production of color, and since the surface composition of all three types of supraballs is dominated by SMPs, their optical response is similar. In contrast to the small variations of colors observed in supraballs, the colors of the scattered light from films are strongly dependent on the bulk volume fraction in the mixtures of SPs and SMPs (Fig. 3, insets, and fig. S5). Therefore, segregation of SMPs to the supraball surfaces offers an effective way of using a small quantity of SMP particles to tune the supraball color without affecting the inner structure of the supraballs.

Driving forces for surface segregation

To explain the observation that both smaller particles and SMPs were strongly enriched at the surface of supraballs but not for films, we used interfacial tension measurements, contact angle measurements of single nanoparticles, and CG-MD simulations. First, we probed the

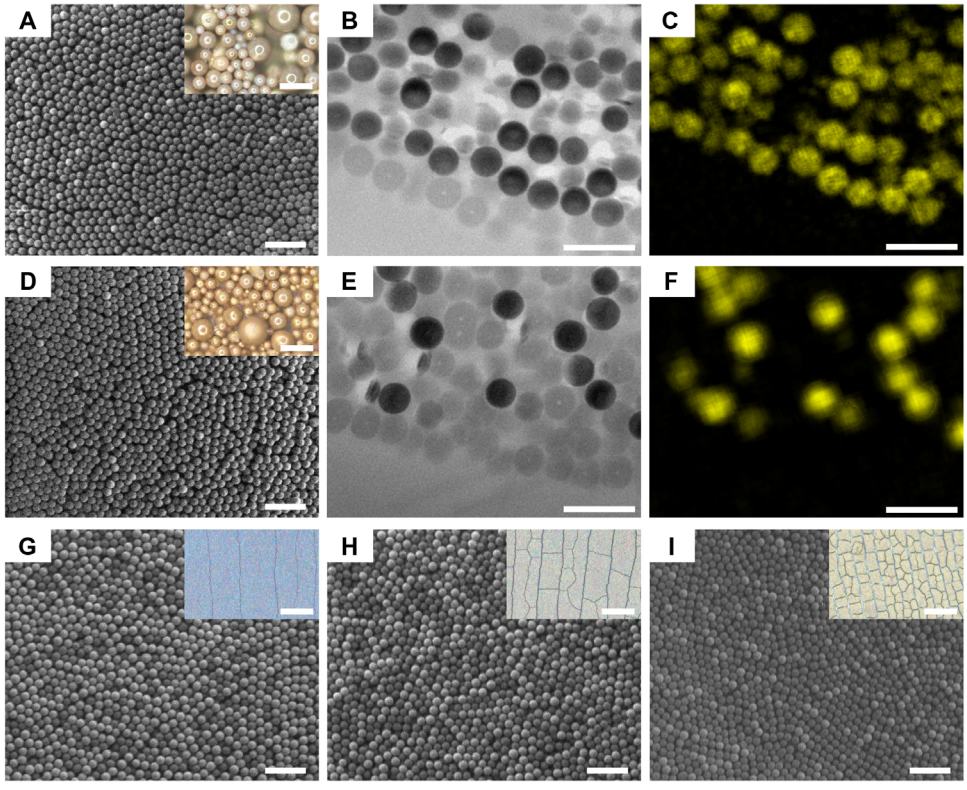

Fig. 3. Supraballs and films assembled from binary 219/217nm SPs/SMPs. Supraballs made of 0.20 bulk volume fraction of SMPs (**A** to **C**) and 0.80 bulk volume fraction of SMPs (**D** to **F**). (A and D) SEM images on the supraball surfaces (scale bars, 1 μm), (B and E) TEM images on the supraball cross sections (scale bars, 500 nm), and (C and F) EDS elemental maps of the region of interest for the characteristic x-ray emission peaks for silicon (scale bars, 500 nm). SEM images on the surfaces of films made of 219/217-nm SPs/SMPs with varied bulk volume fractions of SMPs: (**G**) 0.20, (**H**) 0.50, and (**I**) 0.80. (G and H) Scale bars, 1 μm. Insets in (A), (D), and (G) to (I) are optical images of the supraballs and films with scale bars of 50 μm.

thermodynamic driving forces for assembly of particles at the water/air interface during evaporative film assembly and at the water/1-octanol interface during emulsion assembly by measuring the interfacial tension with and without the presence of particles. We used a pendant droplet method to record the water/air surface tension (γ_{WA}) of 0.03 (filling volume fraction) aqueous suspensions of 219-nm SPs, 217-nm SMPs, and a mixture of SPs and SMPs with the same bulk volume fraction over around 600 s, during which the droplet volumes change negligibly (fig. S6). The γ_{WA} remains almost constant over the time scale of the experiment (fig. S7A) and is similar to the surface tension of pure water (~72 mN/m). This result implies that SPs and SMPs do not adsorb to the water/air interface during the film assembly process (*35*).

In the water/1-octanol system, the interfacial tension γ_{WO} = 8.51 ± 0.02 mN/m for a pure water/1-octanol interface without particles, consistent with the literature value (*36*). However, γ_{WO} decreased notably in the presence of 3 volume % particles: 6.18 ± 0.05 mN/m for SPs and 7.50 ± 0.26 mN/m for SMPs. The values of γ_{WO} remain constant over 600 s in all three cases (fig. S7B). The interfacial tension for the mixture of SPs and SMPs lies between pure SPs and pure SMPs. γ_{WO} slightly decreases from 6.72 ± 0.06 mN/m to 6.53 ± 0.07 mN/m after 1400 s, approaching closer to the γ_{WO} of pure SPs. In short, both SPs and SMPs adsorb to the water/1-octanol interface and that, in a mixture of SPs and SMPs, SPs migrate to the interface over time and reduce the free energy of the water/1-octanol interface to a value closer to pure SPs.

We can use the interfacial tension results to estimate the energy of adsorption of particles to the water/1-octanol interface. The difference between γ values with and without particles represents a change in interfacial energy per unit area upon particle adsorption. If we assume that particles are relatively monodisperse and form a random close-packed monolayer at the interface (surface area coverage, ~80%) (*37*), then the change in surface tension upon particle adsorption is given by (*38*)

$$\Delta\gamma_{WO} = \gamma_{WO+\text{particles}} - \gamma_{WO} = n\Delta E_i \approx \frac{0.8\Delta E_i}{\pi r_i^2} \quad (1)$$

where ΔE_i is the energy of adsorption of a single particle, r_i is the particle radius, and n is the number of particles per unit area of interface ($n \approx 0.8/\pi r_i^2$). Using the γ_{WO} results for ~220-nm-diameter particles gives $\Delta E_i \approx 25{,}000\ k_BT$ for SPs and $\Delta E_i \approx 12{,}000\ k_BT$ for SMPs. Thus, SPs should thermodynamically prefer to migrate to the water/1-octanol interface relative to SMPs, which contradicts our observations that SMPs are dominant at the supraball surface. This suggests that there must be another mechanism underlying the trends in supraball surface segregation.

We hypothesize that during the formation of supraballs, the different surface chemistry of SPs and SMPs also affects the geometric position (i.e., contact angle) of nanoparticles at the water/1-octanol interface, which may affect the surface segregation. The hydrophilicity of particles is closely related to their geometric position at the interface. To directly measure the contact angles of particles at the water/1-octanol interface, we used a gel trapping technique to trap particles at the interface and then transferred the particles to a polydimethylsiloxane (PDMS) matrix (Fig. 4A, see details in Materials and Methods) (*39*, *40*). We measured the height of the particles embedded into PDMS to calculate the contact angle of individual nanoparticles from SEM images (Fig. 4B). Here, we used a larger particle size (~400 nm) than those for supraball assembly to improve the accuracy of our analysis. We used melanin-coated SPs (M-SPs) instead of SMPs because SMPs are not perfectly spherical when we synthesize particles of around 400 nm in diameter. By coating

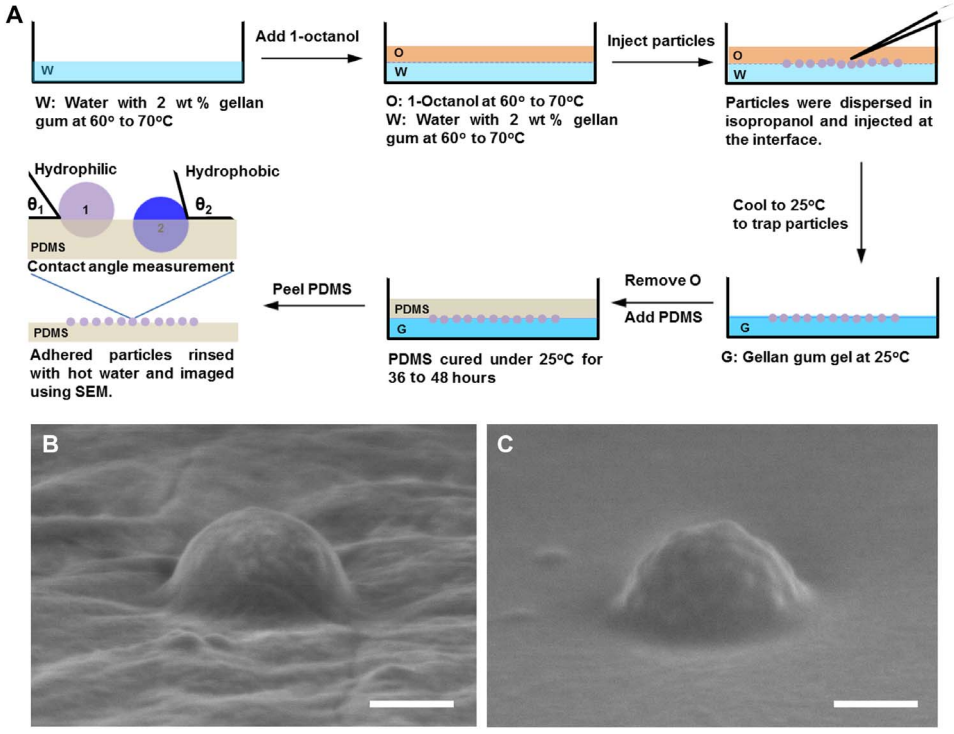

Fig. 4. Single-particle contact angle measurements. (**A**) Schematic diagram of single-nanoparticle contact angle measurement process using a gel trapping technique. SEM images of an SP (**B**) and an M-SP (**C**) embedded in PDMS for contact angle measurements (SP, ~78.4° ± 4.9°; M-SP, ~99.0° ± 3.6°). Scale bars, 200 nm.

melanin layer onto silica nanoparticles, we could maintain the spherical shape of these particles (fig. S8). We expect the surface chemistry of the M-SPs to be similar to the pure SMPs and thus result in the same contact angle. From the image analysis, we measured the contact angle of $\theta_{SP} = 78.4 \pm 4.9°$ and $\theta_{SMP} = \theta_{M\text{-}SP} = 99.0 \pm 3.6°$ for SP and SMP particles, respectively. This result indicates that the SMPs extend less into the water phase, and thus, SMPs are less hydrophilic than SPs. We used CG-MD simulations to evaluate whether this difference in contact angles explains the surface segregation mechanism during supraball assembly.

We used implicit-solvent CG-MD simulations to study the assembled supraball and film structures over experimentally relevant micrometer length scales, which would not be possible using explicit-solvent MD simulation models that have been used to understand particle assembly at liquid/liquid (*41*–*44*) and liquid/vapor interfaces (*45*–*47*) at much smaller length scales. Such implicit-solvent approaches have been widely applied to study stratification in the evaporative film assembly process (*25*, *26*, *31*, *32*), which we adapt to mimic the emulsion assembly. Here, we chose particle-particle and particle-interface interaction potentials to mimic the impact of the solvent and fluid-fluid interfaces on the particle assembly. In the film geometry, we used a repulsive wall at the upper boundary of the simulation box to model the particles' interaction with the water/air interface (as supported by the surface tension results) and shrank the z dimension of the simulation box in a stage-wise manner to mimic evaporation of water from the film (see simulation details in the Supplementary Materials). Simulation images of films composed of ~220-nm SP/SMP mixtures at 0.20, 0.50, and 0.80 bulk volume fraction of SMPs and a ~140-nm SP/~220-nm SP mixture at 0.5 bulk volume fraction of small SPs are shown in Fig. 5 (A to D, respectively) (compared to the experimental images in Figs. 3, G to I, and 2D). The surface volume fraction of SMPs on the top layer of the assembled SP/SMP films in Fig. 5 (A to C) is 0.783 ± 0.003, 0.497 ± 0.003, and 0.213 ± 0.006, and the surface volume fraction of 140-nm SPs in Fig. 5D is 0.502 ± 0.004, in excellent quantitative agreement with the experimental results.

We compared the structure of the top surface of the films using the two-dimensional particle-particle pair correlation function, $g(r)$, which also shows quantitative agreement between simulation and experiment in the SP/SMP mixtures (Fig. 5, E to G, and fig. S9) and the SP/SP mixture (Fig. 5, H to J). When computing the $g(r)$ for simulations containing SMPs, we needed to add a small uncertainty in particle positions to achieve agreement between simulation and experiment, as discussed in the Supplementary Materials (fig. S10). When particles are of similar size (Fig. 5, E to G), the films show some degree of order, whereas when particles are of different size (Fig. 5, H to J), the order is suppressed [the $g(r)$ decays to 1 for interparticle distances greater than one to two particle diameters]. This agreement in both composition and structure at the film surface supports our model for the particle-particle interactions for SP/SMP and SP/SP mixtures and also supports our inference from the surface tension results that neither SPs nor SMPs adsorb to the water/air interface during film assembly.

We then used the model validated for films to conduct simulations in the supraball geometry. In the supraball simulations, the water/1-octanol interface is modeled using a wall defined on the interior surface of a spherical region of the simulation box, and particles are strongly attracted to this wall to mimic the essentially irreversible adsorption of particles to the water/1-octanol interface. While the large particle-interface attraction strengths estimated above ($>10^4\ k_BT$) are not accessible in the simulations to maintain numerical stability, we chose the particle-wall attraction strengths to maintain several key features of particle assembly: (i) particle-wall interaction strength

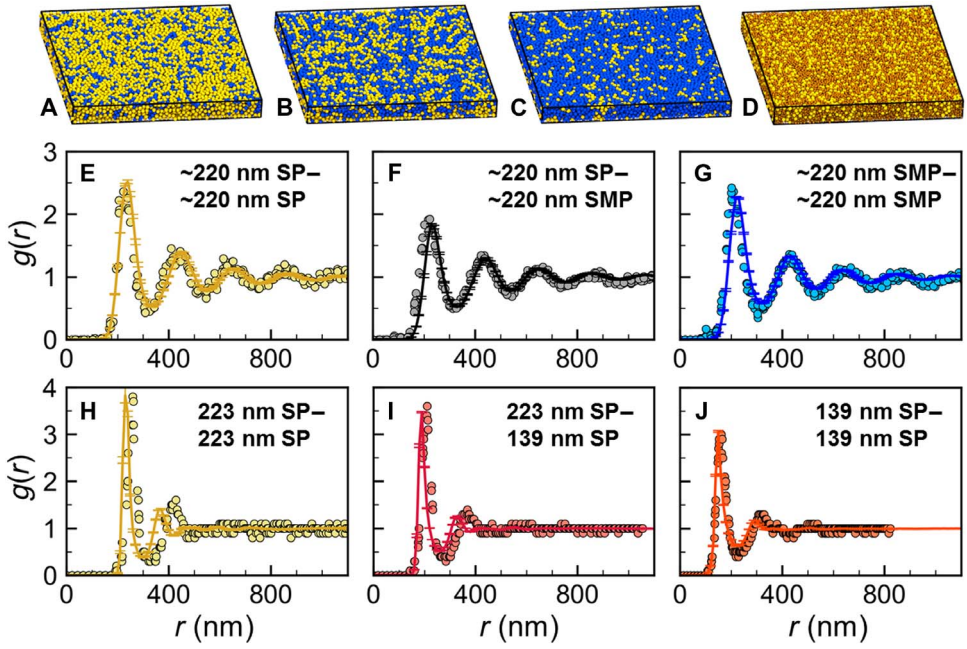

Fig. 5. MD simulations of assembled binary films. (**A** to **D**) MD simulation snapshots for assembled films from similar-sized (~220 nm) SPs (yellow) and SMPs (blue) and mixtures of different sizes of SPs (~220 nm/~140 nm). The bulk volume fractions of SMPs are as follows: (A) 0.20, (B) 0.50, and (C) 0.80. (D) SPs (~220 nm; yellow): ~140-nm SPs (orange) at bulk volume fraction of small SP = 0.5. Particle-particle pair correlation functions, $g(r)$, from experiments (circles) and simulations (lines) for (**E** to **G**) the film pictured in (B) and (**H** to **J**) the film pictured in (D).

scales with r_i^2 (*48*), (ii) SP-wall interactions are ~2× stronger than SMP-wall interactions, and (iii) particle-wall interactions are strong enough (at least 54 k_BT for all particle types and sizes) to mimic irreversible particle adsorption to the interface. Over the course of the simulation, we linearly decrease the diameter of the spherical confinement (D_s) to mimic diffusion of water out of the emulsion droplet, at a rate chosen to match the Péclet number (*Pe*) between simulations and experiments. The *Pe* is a measure of the relative rate of interfacial motion to the rate of particle diffusion. We estimate $Pe \sim 0.1$ for the supraball assembly process as explained in detail in the Supplementary Materials, indicating that particle diffusion is fast relative to the rate of motion of the interface.

The simulations reveal a two-stage assembly mechanism as the emulsion droplet shrinks; we include a representative movie of the assembly simulations in the Supplementary Materials. Starting from a randomized initial configuration at filling volume fraction $\eta = 0.03$ (same initial particle concentration as the experiments), particles diffuse and adsorb to the outer surface of the emulsion droplet until a static (jammed) surface layer of particles assembles at the water/1-octanol interface. Then, as the emulsion droplet continues to shrink, some of the adsorbed particles are squeezed into the bulk of the emulsion droplet to accommodate the reduction in interfacial area and increased curvature of confinement. This process continues until the supraball reaches its final assembled state where η is estimated to be 0.55. The transition between the two stages of assembly is visible in a discontinuity in the slope of the surface volume fraction plots in Fig. 6A; these results show that the second stage is dominant in controlling the eventual supraball surface composition.

Furthermore, in simulations, we can independently tune the particle-interface attraction strength and particle-interface contact angle to test the dominant phenomena controlling the assembly pathway; these tests explain the experimental surface segregation results. When only the particle-interface attraction strength is taken into account (i.e., all particles have the same particle-interface contact angle), the less strongly adsorbed species (SMPs) is squeezed out as the emulsion droplet shrinks, resulting in an SP-rich supraball surface with 0.137 surface volume fraction SMP [Fig. 6, A (solid green line) and B]; this is contrary to the experimental observations. However, when the locations of the particle-interface potentials are adjusted to mimic the measured particle-interface contact angle for the SP (~78.4°) and SMP (~99.0°) chemistries, the SMPs extend further into the 1-octanol phase (see fig. S11). As the interfacial area shrinks, the SMPs squeeze the SPs back toward the bulk of the droplet based on the geometry of their location along the curved water/1-octanol interface (see schematic in fig. S12), resulting in an SMP-rich interface with 0.992 surface volume fraction of SMPs [Fig. 6, A (light blue dashed line) and C]; this agrees with experimentally observed SMP enrichment. The geometry-dominant mechanism occurs despite the fact that the SP-interface attraction strength is 2× higher than the SMPs, which explains why the experimental surface segregation seemingly conflicts with the interfacial tension results. As a control to probe the sensitivity of these results, we tested differences in SP-interface and SMP-interface contact angles as small as 5° and found that even in this case, the particle chemistry with the larger contact angle was enriched at the surface.

In SP mixtures of varying size, as a 140-nm SP:220-nm SP mixture with 0.5 bulk volume fraction of small SPs, we see strong enrichment

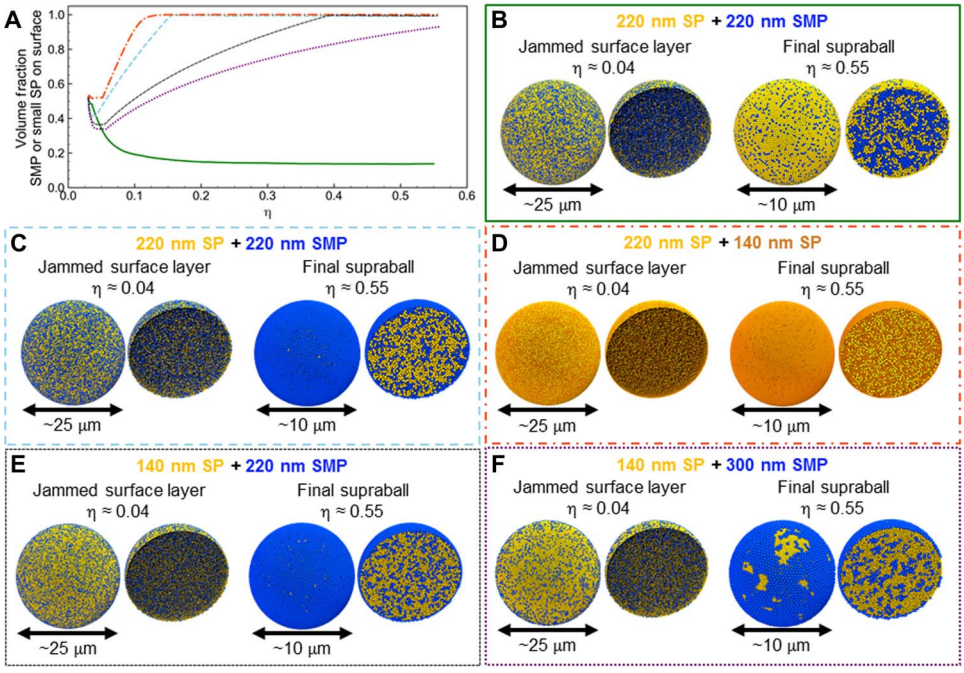

Fig. 6. MD simulations of assembled binary supraballs. (**A**) Surface volume fractions of SMPs or small SPs at the supraball surface as a function of filling volume fraction (η) within the droplet and (**B** to **F**) simulation images for a 220/220-nm SPs/SMPs mixture of the equal bulk volume fractions with $\theta_{SP} = \theta_{SMP} = 90°$ (B) (green solid line), 220/220-nm SPs/SMPs with $\theta_{SP} = 80°$ and $\theta_{SMP} = 100°$ (C) (light blue dashed line), 220/140-nm SPs/SPs with $\theta_{SP} = 80°$ (D) (orange dot-dashed line), 140/220-nm SPs/SMPs with $\theta_{SP} = 80°$ and $\theta_{SMP} = 100°$ (E) (thin black dashed line), and 140/300-nm SPs/SMPs with $\theta_{SP} = 80°$ and $\theta_{SMP} = 100°$ (F) (purple dotted line). The two left images in (B) to (D) show the entire emulsion droplet and a droplet cross section at the jammed surface layer state, and the two right images in (B) to (D) show the final assembled supraball and supraball cross section. SMPs are rendered in blue, and SPs are rendered in yellow in all panels except for (D), where 140-nm SPs are rendered in orange for visual contrast. The boxes surrounding (B) to (D) correspond to the line color and type in (A). The simulation images are not to scale.

of the smaller SPs [Fig. 6, A (orange dot-dashed line) and D] due to the smaller particles' improved ability to accommodate the curvature of the supraball surface. We note that the supraball surface stratification in the 140-nm SP:200-nm SP simulations (surface volume fraction of small SP, ~0.999) is stronger than that seen in the experiments (surface volume fraction of small SP, ~0.89; Fig. 2, A and G). We hypothesize that this quantitative difference in the degree of size segregation could be a combination of two effects. First, our CG-MD approach neglects the hydrodynamics of the water diffusing out of the emulsion droplet; recent work on films suggests that this methodological choice can affect the degree of segregation predicted (*49*). However, explicitly including the hydrodynamics would not be computationally feasible at the (relatively) large length and time scales probed in this work. Secondly, in our simulations, the liquid/liquid interface is modeled by a perfectly spherical rigid wall, whereas in the experimental system, the interface may be perturbed by the presence of particles.

Lastly, simulation results for SP/SMP mixtures of varying size are shown in Fig. 6 (A, E, and F). These results match the experimental trends shown in Fig. 1, in that an increasing fraction of SP particles remain at the supraball surface as the SPs become smaller than SMPs. In the simulations, the 140/220-nm SP/SMP mixture had a final 0.993 surface volume fraction of SMPs, and the 140/300-nm SP/SMP mixture had a final 0.930 surface volume fraction of SMPs. This is due to a competition between the chemistry/contact angle effect, which drives SMPs to the supraball surface, and the particle size effect, which drives small particles to the supraball surface. Comparing the simulation images in Fig. 6 (E and F) to the SEM images in Fig. 1 (D and G), the experiments exhibit a higher degree of mixing of SPs and SMPs than seen in the simulations. This discrepancy is expected, given that the model was parameterized to match the structure of the 220-nm SP:220-nm SMP system and used without adjustments for the other particle mixtures. However, we emphasize that the qualitative trends in surface composition as a function of size and particle chemistry agree between both simulations and experiments, thus solidifying our explanation of the assembly mechanism.

CONCLUSIONS

In summary, we studied the surface packing and structural colors of reverse emulsion assembled supraballs and evaporative assembled films using binary mixtures of SPs and SMPs. We demonstrate that smaller particles prefer to stay at the supraball surface and that SMPs preferentially segregate at the surface more than SPs. By contrast, small particles or SMPs do not preferentially segregate at the film interfaces for the moderate size ratios studied herein. This selective surface enrichment of particles in the supraballs leads to unique control of structural colors compared to films. We further use interfacial tension and particle contact angle measurements combined with CG-MD simulations to demonstrate that the key difference between self-assembly in supraballs and films is the combination of particle-interface contact angle and the decreasing interfacial area during the emulsion assembly. We show that in the regime studied herein, where all particles irreversibly adsorb to the water/1-octanol interface, particles with a higher particle-interface contact angle preferentially segregate to the supraball surface owing to a geometric "squeezing" mechanism during the assembly, and this effect dominates over any potential differences in particle-interface attraction strength. Conversely, since the film drying process does not involve a reduction of interfacial area over time, there is not a strong driving force for surface segregation, producing a film surface composition similar to the bulk.

This work demonstrates that the tunability of particle packing using different particle sizes, different particle chemistries, or different assembly methods offers new opportunities to produce desired colors or gradient surface properties for coatings. In addition, the use of SP/SMP mixtures has several advantages for preparing assembled photonic materials. Melanin has a unique combination of broadband absorption and high refractive index, and the use of SMPs in the supraballs largely enhances the color saturation. On the basis of our results, we infer that one can reduce the amount of SMPs used to prepare supraballs without losing color saturation since SMPs preferentially stay at the supraball surfaces. In the future, we envision expanding the application of our supraball systems by etching away inner SPs to make permeable melanin colloidal capsules that potentially find uses as drug delivery or scaffold materials.

MATERIALS AND METHODS

Supraball and film preparation

SPs were synthesized using a modified Stöber process (*50*). SMPs were prepared by oxidation and polymerization of dopamine (Sigma-Aldrich) in a mixture of water, ethanol, and ammonia hydroxide at room temperature following our previous reported protocol (*33*). Particle sizes were controlled by changing the amount of ammonium hydroxide (28 to 30% wt %; Sigma-Aldrich). We followed our previous reverse emulsion assembly protocol to make binary supraballs (*11*). Typically, we added 30 μl of aqueous solution of SPs/SMPs (filling volume fraction 3%) into 1 ml of anhydrous 1-octanol (Sigma-Aldrich). We used a vortex to shake the mixture to form reverse emulsion at a speed of 1600 rpm for 2 min and then 1000 rpm for 3 min. After supraball particles precipitated, we removed the supernatant and dried the samples under 60°C.

We used an evaporative assembly method to make films from mixtures of SP and SMP solutions (*6*). Typically, we prepared a solution of mixed SPs and SMPs at a filling volume fraction of 0.5%. A clean silicon wafer was vertically immersed into a suspension bath, and particles were deposited onto the clean silicon wafer to form films when the water evaporated at 60°C overnight. The water evaporating rate was recorded to be 0.5 mm/hour by tracking the decrease of water height in the container.

Sample characterization

Dried supraball powders and films were directly imaged using an Olympus BX 51 microscope under the dark-field mode. Here, we used white Teflon tape as a white standard. We measured reflectance spectra of single supraballs and films using a CRAIC AX10 ultraviolet-visible-near-infrared microspectrophotometer (CRAIC Technologies Inc.). We used a 50× objective and a 75-W Xenon short arc lamp (Ushio UXL-75XE) for the light source. We reported the averaged spectra from six measurements using pavo package in R programming software (*51*).

We combined SEM and TEM to investigate the distribution of SPs and SMPs in the photonic assemblies. We imaged the surface of both supraballs and films using an SEM (JEOL-7401, JEOL Ltd) without any sputter-coating to maintain the inherent contrast from SMPs and SPs. To quantify the SEM images, we used a MATLAB code [*imfindcircles* (*52*)] for images containing different sizes of particles and a python code [*Trackpy* (*53*)] for images containing particles with different

brightness. Using these centers and radii, we plotted the measured circles over the original image to ensure that this analysis captured the real features of particles (fig. S13). The output of running these algorithms was a list of particle sizes and positions within each image, which we used to calculate the surface volume fraction and $g(r)$ for the surface layer. To prepare thin cross sections of supraballs for TEM imaging, we embedded dried supraball powders with EMbed 812 resin and cut the samples to 80-nm-thick sections using a diamond knife on a Leica UC7 ultramicrotome. TEM images and EDS elemental map were acquired using a Hitachi HD-2300 Dual EDS Cryo STEM equipped with dual Thermo Fisher Scientific (Waltham, MA) EDS detectors (total x-ray collection angle, ~0.8 steradian). Both TEM images and EDS data were obtained using Thermo Fisher Scientific NSS software under EDX operation mode and TE mode (phase contrast mode).

Interfacial tension measurement

We used pendant droplet methods to measure the interfacial tension between aqueous colloidal solutions and 1-octanol and the surface tension of aqueous colloidal solutions. The filling volume fraction of colloids is 0.03, which was the same as that used for supraball assembly. Here, we used 219-nm SPs and 217-nm SMPs. For the surface tension measurements, we opened the droplet in a quartz cuvette to reduce evaporation. In the interfacial tension measurements, we made a saturated 1-octanol solution with an excess amount of water and then opened the aqueous droplet (with or without particles) in the saturated 1-octanol solution, so that there is little water diffusion into 1-octanol. We recorded the interfacial tension values and the droplet volume over a period of time (600 or 1400 s). The volume of droplets did not change, and thus the diffusion of water into 1-octanol (or vice versa) was negligible during the time scale of our measurements (fig. S6). As a control, we also measured interfacial tension between water and 1-octanol without any colloids.

Contact angle of single nanoparticle measurement and calculation

We used a gel trapping technique to trap the particle at the water/1-octanol interface and analyzed the contact angle value of single nanoparticles with the help of SEM characterization and ImageJ analysis (*39*, *40*). See Fig. 4A for a schematic of the gel trapping process. Specifically, gellan gum (2 wt %) was dispersed in water (10 ml) and heated to 60° to 70°C for 30 min to fully dissolve. The gelation temperature of 2 wt % gellan gum was 40° to 45°C. We preheated both 1-octanol (3 ml) and colloidal isopropanol suspension (SPs and M-SPs with diameter around ~400 nm, 0.5 mg/ml). Isopropanol was used as a spreading solvent to help particles disperse at the interface. Then, 1-ocatanol was added into gellan gum solution, followed by injection of the particle suspension into the water/1-octanol interface. Upon cooling to room temperature around 25°C, the gellan gum solution began to gel and was kept for another 30 min. 1-Octanol, existing on the top layer, was then carefully removed. PDMS (SYLGARD 184 Silicone Elastomer, Dow Corning) was mixed in a ratio of 10:1 and degassed before being layered over the gelled gellan gum. After PDMS was cured for 36 to 48 hours at room temperature, it was peeled off (with particles adhered to the PDMS surface) and rinsed with hot water (60° to 70°C) to wash away gellan gum residue. We coated particle-embedded PDMS with ~9 nm of osmium for SEM characterization. ROI (Region of Interest) manager in ImageJ was used to analyze the SEM images and measure how deeply particles were embedded in PDMS for the contact angle calculation. For each type of particle, we measured 10 particles to obtain an average value and standard deviation.

CG-MD simulations

We performed implicit-solvent CG Langevin dynamics simulations in the isochoric-isothermal (NVT) ensemble using LAMMPS software package (*54*). The SPs and SMPs are represented as spheres with particle-particle interactions modeled using the colloid Lennard-Jones (LJ) potential (*55*), with particle-particle interaction strength, particle size and size dispersity, and particle masses chosen to reproduce the experimental structure of SP/SMP films. In the film geometry, we modeled particle-substrate interactions at the $z = 0$ surface of the simulation box with the 9-3 LJ potential, and we represented particle interactions with the water/air interface with a repulsive harmonic potential at the top of the simulation box. In the supraball geometry, we defined a spherical region of diameter D_s to mimic the outer surface of the emulsion droplet, and we modeled attractive interactions with this water/1-octanol interface with the 9-3 LJ potential. We chose the water/1-octanol particle-interface interaction strength, $\varepsilon_{P\text{-}I}$, to mimic the irreversible adsorption of particles to the interface; $\varepsilon_{P\text{-}I}$ ranged from 54 to 278 k_BT depending on the particle size and chemistry. All parameters governing the particle-particle and particle-interface interactions are listed in the Supplementary Materials, and schematics of the simulation box geometries are given in fig. S14.

For the film simulations, we performed a slow stage-wise increase in filling volume fraction η, as the simulation proceeded to mimic the increasing η in the film due to evaporation of water during the thin-film assembly process (mimicking an evaporation $Pe \rightarrow 0$). For the supraball simulations, we started from a randomized initial configuration at an initial $\eta = 0.03$ and then enabled the attractive particle-interface interactions and decreased D_s to model the shrinkage of the emulsion droplet as assembly proceeds. The rate of change of D_s was chosen to match the emulsion assembly Pe between simulation and experiments around $Pe \sim 0.1$. Full details of the simulation and analysis methodologies for the film and supraball simulations are given in the Supplementary Materials.

SUPPLEMENTARY MATERIALS

Supplementary material for this article is available at http://advances.sciencemag.org/cgi/content/full/5/9/eaax1254/DC1

CG-MD simulations model and methods

Table S1. Zeta potentials and diameters of all six types of particles.

Fig. S1. The workflow for preparing the binary supraballs.

Fig. S2. Normal reflectance of nine types of supraballs in Fig. 1.

Fig. S3. An SEM image of a typical broken film made of a mixture of 139- and 219-nm SPs.

Fig. S4. Cross-sectional images of supraballs (interior) made of 219-nm SPs and 217-nm SMPs with varied mixing volume ratios.

Fig. S5. Normal reflectance measurements of binary supraball and films.

Fig. S6. The volume changes of different droplets over time during the pendant droplet measurements.

Fig. S7. Surface and interfacial tension measurements.

Fig. S8. TEM images of ~400-nm SPs and M-SPs.

Fig. S9. Particle-particle pair correlation functions from experiment (circles) and simulations (lines) for films made of ~220-nm SP/SMPs mixtures.

Fig. S10. Particle-particle pair correlation functions from simulations for a binary SP/SMP film with (solid lines) and without (dashed lines) a 17-nm Gaussian uncertainty in particle *x-y* positions.

Fig. S11. Illustration of particle-interface potential for 220-nm SPs (yellow solid line) and 220-nm SMPs (blue dashed line).

Fig. S12. Schematic of the later stages of supraball assembly.

Fig. S13. Examples of particle position tracking analysis on SEM images.

Fig. S14. Schematic of the simulation box geometry for film and supraball assembly.
Fig. S15. Distributions of particle sizes and their effect on the particle-particle pair correlation function in simulations.
Fig. S16. *Pe* effect on the simulations.
Movie S1. A representative movie of the supraball assembly simulations.
References (*56*, *57*)

REFERENCES AND NOTES

1. Y. Zhai, Y. Ma, S. N. David, D. Zhao, R. Lou, G. Tan, R. Yang, X. Yin, Scalable-manufactured randomized glass-polymer hybrid metamaterial for daytime radiative cooling. *Science* **355**, 1062–1066 (2017).
2. H.-N. Kim, S. Vahidinia, A. L. Holt, A. M. Sweeney, S. Yang, Geometric design of scalable forward scatterers for optimally efficient solar transformers. *Adv. Mater.* **29**, 1702922 (2017).
3. H. Inan, M. Poyraz, F. Inci, M. A. Lifson, M. Baday, B. T. Cunningham, U. Demirci, Photonic crystals: Emerging biosensors and their promise for point-of-care applications. *Chem. Soc. Rev.* **46**, 366–388 (2017).
4. M. Fanun, *Colloids in Drug Delivery* (CRC Press, ed. 1, 2016).
5. J. F. Galisteo-López, M. Ibisate, R. Sapienza, L. S. Froufe-Pérez, Á. Blanco, C. López, Self-assembled photonic structures. *Adv. Mater.* **23**, 30–69 (2011).
6. M. Xiao, Y. Li, J. Zhao, Z. Wang, M. Gao, N. C. Gianneschi, A. Dhinojwala, M. D. Shawkey, Stimuli-responsive structurally colored films from bioinspired synthetic melanin nanoparticles. *Chem. Mater.* **28**, 5516–5521 (2016).
7. B. Hatton, L. Mishchenko, S. Davis, K. H. Sandhage, J. Aizenberg, Assembly of large-area, highly ordered, crack-free inverse opal films. *Proc. Natl. Acad. Sci. U.S.A.* **107**, 10354–10359 (2010).
8. A. L. Rogach, N. A. Kotov, D. S. Koktysh, J. W. Ostrander, G. A. Ragoisha, Electrophoretic deposition of latex-based 3D colloidal photonic crystals: A technique for rapid production of high-quality opals. *Chem. Mater.* **12**, 2721–2726 (2000).
9. Y. Takeoka, S. Yoshioka, A. Takano, S. Arai, K. Nueangnoraj, H. Nishihara, M. Teshima, Y. Ohtsuka, T. Seki, Production of colored pigments with amorphous arrays of black and white colloidal particles. *Angew. Chem. Int. Ed.* **52**, 7261–7265 (2013).
10. Y. Zhao, L. Shang, Y. Cheng, Z. Gu, Spherical colloidal photonic crystals. *Acc. Chem. Res.* **47**, 3632–3642 (2014).
11. M. Xiao, Z. Hu, Z. Wang, Y. Li, A. D. Tormo, N. Le Thomas, B. Wang, N. C. Gianneschi, M. D. Shawkey, A. Dhinojwala, Bioinspired bright noniridescent photonic melanin supraballs. *Sci. Adv.* **3**, e1701151 (2017).
12. C. Zhu, W. Xu, L. Chen, W. Zhang, H. Xu, Z.-Z. Gu, Magnetochromatic microcapsule arrays for displays. *Adv. Funct. Mater.* **21**, 2043–2048 (2011).
13. S.-H. Kim, J.-G. Park, T. M. Choi, V. N. Manoharan, D. A. Weitz, Osmotic-pressure-controlled concentration of colloidal particles in thin-shelled capsules. *Nat. Commun.* **5**, 3068 (2014).
14. J. Cui, W. Zhu, N. Gao, J. Li, H. Yang, Y. Jiang, P. Seidel, B. J. Ravoo, G. Li, Inverse opal spheres based on polyionic liquids as functional microspheres with tunable optical properties and molecular recognition capabilities. *Angew. Chem. Int. Ed.* **53**, 3844–3848 (2014).
15. P. D. García, R. Sapienza, C. López, Photonic glasses: A step beyond white paint. *Adv. Mater.* **22**, 12–19 (2010).
16. J. D. Forster, H. Noh, S. F. Liew, V. Saranathan, C. F. Schreck, L. Yang, J.-G. Park, R. O. Prum, S. G. Mochrie, C. S. O'Hern, E. R. Dufresne, Biomimetic isotropic nanostructures for structural coloration. *Adv. Mater.* **22**, 2939–2944 (2010).
17. G. Singh, S. Pillai, A. Arpanaei, P. Kingshott, Multicomponent colloidal crystals that are tunable over large areas. *Soft Matter* **7**, 3290–3294 (2011).
18. A. Kawamura, M. Kohri, S. Yoshioka, T. Taniguchi, K. Kishikawa, Structural color tuning: Mixing melanin-like particles with different diameters to create neutral colors. *Langmuir* **33**, 3824–3830 (2017).
19. P. D. García, R. Sapienza, C. Toninelli, C. López, D. S. Wiersma, Photonic crystals with controlled disorder. *Phys. Rev. A* **84**, 023813 (2011).
20. A. R. Bausch, M. J. Bowick, A. Cacciuto, A. D. Dinsmore, M. F. Hsu, D. R. Nelson, M. G. Nikolaides, A. Travesset, D. A. Weitz, Grain boundary scars and spherical crystallography. *Science* **299**, 1716–1718 (2003).
21. G. Meng, J. Paulose, D. R. Nelson, V. N. Manoharan, Elastic instability of a crystal growing on a curved surface. *Science* **343**, 634–637 (2014).
22. R. Chen, D. J. G. Pearce, S. Fortuna, D. L. Cheung, S. A. Bon, Polymer vesicles with a colloidal armor of nanoparticles. *J. Am. Chem. Soc.* **133**, 2151–2153 (2011).
23. N. Vogel, S. Utech, G. T. England, T. Shirman, K. R. Phillips, N. Koay, I. B. Burgess, M. Kolle, D. A. Weitz, J. Aizenberg, Color from hierarchy: Diverse optical properties of micron-sized spherical colloidal assemblies. *Proc. Natl. Acad. Sci. U.S.A.* **112**, 10845–10850 (2015).
24. R. Tang, C. S. Kim, D. J. Solfiell, S. Rana, R. Mout, E. M. Velázquez-Delgado, A. Chompoosor, Y. Jeong, B. Yan, Z.-J. Zhu, C. Kim, J. A. Hardy, V. M. Rotello, Direct delivery of functional proteins and enzymes to the cytosol using nanoparticle-stabilized nanocapsules. *ACS Nano* **7**, 6667–6673 (2013).
25. A. Fortini, I. Martín-Fabiani, J. L. De La Haye, P.-Y. Dugas, M. Lansalot, F. D'Agosto, E. Bourgeat-Lami, J. L. Keddie, R. P. Sear, Dynamic stratification in drying films of colloidal mixtures. *Phys. Rev. Lett.* **116**, 118301 (2016).
26. M. P. Howard, A. Nikoubashman, A. Z. Panagiotopoulos, Stratification dynamics in drying colloidal mixtures. *Langmuir* **33**, 3685–3693 (2017).
27. Y. Tang, G. S. Grest, S. Cheng, Stratification in drying films containing bidisperse mixtures of nanoparticles. *Langmuir* **34**, 7161–7170 (2018).
28. R. P. Sear, Stratification of mixtures in evaporating liquid films occurs only for a range of volume fractions of the smaller component. *J. Chem. Phys.* **148**, 134909 (2018).
29. M. Schulz, J. L. Keddie, A critical and quantitative review of the stratification of particles during the drying of colloidal films. *Soft Matter* **14**, 6181–6197 (2018).
30. J. Zhou, Y. Jiang, M. Doi, Cross interaction drives stratification in drying film of binary colloidal mixtures. *Phys. Rev. Lett.* **118**, 108002 (2017).
31. R. Tatsumi, T. Iwao, O. Koike, Y. Yamaguchi, Y. Tsuji, Effects of the evaporation rate on the segregation in drying bimodal colloidal suspensions. *Appl. Phys. Lett.* **112**, 053702 (2018).
32. D. K. Makepeace, A. Fortini, A. Markov, P. Locatelli, C. Lindsay, S. Moorhouse, R. Lind, R. P. Sear, J. L. Keddie, Stratification in binary colloidal polymer films: Experiment and simulations. *Soft Matter* **13**, 6969–6980 (2017).
33. M. Xiao, Y. Li, M. C. Allen, D. D. Deheyn, X. Yue, J. Zhao, N. C. Gianneschi, M. D. Shawkey, A. Dhinojwala, Bio-inspired structural colors produced *via* self-assembly of synthetic melanin nanoparticles. *ACS Nano* **9**, 5454–5460 (2015).
34. Z. Knittl, *Optics of Thin Films: An Optical Multilayer Theory* (Wiley, 1976), vol. 1.
35. T. Okubo, Surface tension of structured colloidal suspensions of polystyrene and silica spheres at the air-water interface. *J. Colloid Interface Sci.* **171**, 55–62 (1995).
36. A. H. Demond, A. S. Lindner, Estimation of interfacial tension between organic liquids and water. *Environ. Sci. Technol.* **27**, 2318–2331 (1993).
37. S. Meyer, C. Song, Y. Jin, K. Wang, H. A. Makse, Jamming in two-dimensional packings. *Physica A* **389**, 5137–5144 (2010).
38. K. Du, E. Glogowski, T. Emrick, T. P. Russell, A. D. Dinsmore, Adsorption energy of nano- and microparticles at liquid–liquid interfaces. *Langmuir* **26**, 12518–12522 (2010).
39. V. N. Paunov, Novel method for determining the three-phase contact angle of colloid particles adsorbed at air-water and oil-water interfaces. *Langmuir* **19**, 7970–7976 (2003).
40. Y. Song, X. Li, J.-B. Fan, H. Kang, X. Zhang, C. Chen, X. Liang, S. Wang, Interfacially polymerized particles with heterostructured nanopores for glycopeptide separation. *Adv. Mater.* **30**, 1803299 (2018).
41. F. Bresme, N. Quirke, Nanoparticulates at liquid/liquid interfaces. *Phys. Chem. Chem. Phys.* **1**, 2149–2155 (1999).
42. M. Luo, O. A. Mazyar, Q. Zhu, M. W. Vaughn, W. L. Hase, L. L. Dai, Molecular dynamics simulation of nanoparticle self-assembly at a liquid–liquid interface. *Langmuir* **22**, 6385–6390 (2006).
43. M. Luo, L. L. Dai, Molecular dynamics simulations of surfactant and nanoparticle self-assembly at liquid–liquid interfaces. *J. Phys. Condens. Matter* **19**, 375109 (2007).
44. H. Fan, A. Striolo, Nanoparticle effects on the water-oil interfacial tension. *Phys. Rev. E* **86**, 051610 (2012).
45. F. Bresme, N. Quirke, Computer simulation study of the wetting behavior and line tensions of nanometer size particulates at a liquid-vapor interface. *Phys. Rev. Lett.* **80**, 3791–3794 (1998).
46. S. Cheng, G. S. Grest, Structure and diffusion of nanoparticle monolayers floating at liquid/vapor interfaces: A molecular dynamics study. *J. Chem. Phys.* **136**, 214702 (2012).
47. S. Cheng, G. S. Grest, Molecular dynamics simulations of evaporation-induced nanoparticle assembly. *J. Chem. Phys.* **138**, 064701 (2013).
48. A. Boker, J. He, T. Emrick, T. P. Russell, Self-assembly of nanoparticles at interfaces. *Soft Matter* **3**, 1231–1248 (2007).
49. A. Statt, M. P. Howard, A. Z. Panagiotopoulos, Influence of hydrodynamic interactions on stratification in drying mixtures. *J. Chem. Phys.* **149**, 024902 (2018).
50. W. Stöber, A. Fink, E. Bohn, Controlled growth of monodisperse silica spheres in the micron size range. *J. Colloid Interface Sci.* **26**, 62–69 (1968).
51. R. Maia, C. M. Eliason, P.-P. Bitton, S. M. Doucet, M. D. Shawkey, pavo: An R package for the analysis, visualization and organization of spectral data. *Methods Ecol. Evol.* **4**, 906–913 (2013).
52. T. J. Atherton, D. J. Kerbyson, Size invariant circle detection. *Image Vis. Comput.* **17**, 795–803 (1999).
53. J. C. Crocker, D. G. Grier, Methods of digital video microscopy for colloidal studies. *J. Colloid Interface Sci.* **179**, 298–310 (1996).
54. S. Plimpton, Fast parallel algorithms for short-range molecular dynamics. *J. Comput. Phys.* **117**, 1–19 (1995).
55. R. Everaers, M. R. Ejtehadi, Interaction potentials for soft and hard ellipsoids. *Phys. Rev. E* **67**, 041710 (2003).
56. T. Schneider, E. Stoll, Molecular-dynamics study of a three-dimensional one-component model for distortive phase transitions. *Phys. Rev. B* **17**, 1302–1322 (1978).

57. W. Humphrey, A. Dalke, K. Schulten, VMD: Visual molecular dynamics. *J. Mol. Graph.* **14**, 33–38 (1996).

Acknowledgments: We thank R. Bleher for assistance in EDS imaging and J. Ricouvier for discussions on the matlab code. **Funding:** We acknowledge support from the Air Force Office of Scientific Research (MURI-FA 9550-18-1-0142, FA9550-18-1-0477, and FA9550-13-1-0222), the National Science Foundation (EAR-1251895, DMR-1105370, and DMR-1609543), and Research Foundation—Flanders (FWO G007117 N). This work made use of the BioCryo facility of Northwestern University's NUANCE Center, which has received support from the Soft and Hybrid Nanotechnology Experimental (SHyNE) Resource (NSF ECCS-1542205); the MRSEC program (NSF DMR-1720139) at the Materials Research Center; the International Institute for Nanotechnology (IIN); and the State of Illinois, through the IIN. This research was supported in part through the use of computational resources from the University of Delaware (Farber cluster) and the Extreme Science and Engineering Discovery Environment (XSEDE) Stampede cluster (allocation MCB100140), which is supported by NSF grant ACI-1548562. **Author contributions:** M. X., A. D., Z. H., and M. D. S. designed the experiments; M. X., Z. H., X.Y., W. L., and M. D. S. conducted the experiments; T. E. G. and A. J. designed and ran the simulations; all authors analyzed data and wrote the paper. **Competing interests:** The authors declare that they have no competing interests. **Data and materials availability:** All data needed to evaluate the conclusions in the paper are present in the paper and/or the Supplementary Materials. Additional data related to this paper may be requested from the authors.

Submitted 24 February 2019
Accepted 20 August 2019
Published 20 September 2019
10.1126/sciadv.aax1254

Citation: M. Xiao, Z. Hu, T. E. Gartner, X. Yang, W. Li, A. Jayaraman, N. C. Gianneschi, M. D. Shawkey, A. Dhinojwala, Experimental and theoretical evidence for molecular forces driving surface segregation in photonic colloidal assemblies. *Sci. Adv.* **5**, eaax1254 (2019).

ScienceAdvances

Experimental and theoretical evidence for molecular forces driving surface segregation in photonic colloidal assemblies

Ming Xiao, Ziying Hu, Thomas E. Gartner III, Xiaozhou Yang, Weiyao Li, Arthi Jayaraman, Nathan C. Gianneschi, Matthew D. Shawkey and Ali Dhinojwala

Sci Adv **5** (9), eaax1254.
DOI: 10.1126/sciadv.aax1254